

PocketGS: On-Device Training of 3D Gaussian Splatting for High Perceptual Modeling

Wenzhi Guo, Guangchi Fang, Shu Yang, Bing Wang*



Fig. 1: Our PocketGS enables high-quality end-to-end 3DGS reconstruction on commodity smartphones. Compared to standard 3DGS workstation baselines, PocketGS achieves superior visual fidelity (LPIPS: 0.108) within a tight training budget (500 iterations, ~ 4 minutes on an iPhone 15).

Abstract—Efficient and high-fidelity 3D scene modeling is a long-standing pursuit in computer graphics. While recent 3D Gaussian Splatting (3DGS) methods achieve impressive real-time modeling performance, they rely on resource-unconstrained training assumptions that fail on mobile devices, which are limited by minute-scale training budgets and hardware-available peak-memory. We present PocketGS, a mobile scene modeling paradigm that enables on-device 3DGS training under these tightly coupled constraints while preserving high perceptual fidelity. Our method resolves the fundamental contradictions of standard 3DGS through three co-designed operators: \mathcal{G} builds geometry-faithful point-cloud priors; \mathcal{I} injects local surface statistics to seed anisotropic Gaussians, thereby reducing early conditioning gaps; and \mathcal{T} unrolls alpha compositing with cached intermediates and index-mapped gradient scattering for stable mobile backpropagation. Collectively, these operators satisfy the competing requirements of training efficiency, memory compactness, and modeling fidelity. Extensive experiments demonstrate that PocketGS is able to outperform the powerful mainstream workstation 3DGS baseline to deliver high-quality reconstructions, enabling a fully on-device, practical capture-to-rendering workflow.

Index Terms—3D Gaussian Splatting, Rendering, on-device, modeling system.

I. INTRODUCTION

3D Gaussian Splatting (3DGS) [1] is a promising paradigm for high-quality scene modeling, advancing mixed reality [2], [3], digital twins [4], [5], and robotic simulation [6], [7]. By

replacing implicit neural representations [8] with rasterization-friendly 3D Gaussians, it achieves real-time high-fidelity modeling, but still suffers from high computation, memory overhead, and training time, hindering on-device training for mobile 3D content creation.

Training 3DGS on device introduces substantial challenges, as it must deliver high perceptual quality under the limited computational resources and strict thermal constraints of mobile platforms. Consequently, the training process must meet **on-device constraints**: 1) completion within a few minutes (e.g., < 5 min), 2) respecting the hardware-available memory budget (e.g., < 3 GB).

These constraints require rethinking 3DGS under resource-limited regimes beyond conventional resource-unconstrained assumptions. Gaussian-based modeling typically includes: (1) recovering camera parameters and a point cloud from images, (2) initializing 3D Gaussians from this geometry, and (3) optimizing the Gaussians via differentiable rendering for scene recovery. Existing designs assume ample time and memory across all stages, but on-device settings break these assumptions, yielding three tightly coupled contradictions. 21

Input-Recovery Contradiction. A primary limitation of on-device 3DGS arises from the contradiction between unreliable geometric input and accurate scene recovery. Mobile scans provide coarse geometry as imprecise poses and sparse points, causing noisy initialization. Existing methods compensate by densifying Gaussians, but this raises computation

and memory overhead, leading to long training times and memory overflow. *Consequently, on-device 3DGS requires reliable geometric input to minimize reliance on excessive densification for scene recovery.*

Initialization-Convergence Contradiction. Another key limitation lies in the contradiction between heuristic initialization and stable convergence. Existing methods disregard geometric priors and initialize input points as isotropic 3D Gaussians, relying on prolonged optimization to compensate for the resulting deficiencies. Under on-device constraints, extra iterations are costly and violate time, energy, and thermal budgets. *Thus, on-device 3DGS requires geometry-conditioned initialization to reduce optimization burden, thereby facilitating stable convergence.*

Hardware-Differentiability Mismatch. On-device 3DGS conflicts with mobile execution: while differentiable splatting needs per-step alpha-compositing states for backpropagation, mobile fixed-function pipelines expose only the final blended color and conceal the depth-ordered accumulation needed to route gradients. Recovering these states via framebuffer read-backs, full buffer clears, or backward-time re-enumeration of per-pixel splat sequences is bandwidth-prohibitive and poorly aligned with mobile GPU state. *Thus, on-device 3DGS calls for a mobile-oriented differentiable rendering framework that explicitly unrolls compositing and replays only the minimal cached intermediates required for Gaussian optimization.*

In this work, we present **PocketGS**, a 3DGS training paradigm that achieves high-perceptual modeling under on-device constraints via three co-designed operators (Fig. 1,2). To address the Input-Recovery Contradiction, the geometry-prior construction operator \mathcal{G} builds a geometry-faithful prior, providing the required geometric guidance without costly in-loop Gaussian densification beyond the on-device envelope. To resolve the Initialization-Convergence Contradiction, the prior-conditioned Gaussian parameterization operator \mathcal{I} uses this prior to shape initial Gaussians, improving conditioning for stable, iteration-limited optimization and reducing degradation from noise-sensitive initialization. Finally, to overcome the Hardware-Differentiability Contradiction, the hardware-aligned splatting optimization operator \mathcal{T} makes differentiable rendering practical on mobile GPUs, preserving correct gradients and stable updates without prohibitive memory traffic. Extensive experiments show that PocketGS achieves perceptual quality superior to mainstream workstation 3DGS baselines, while operating within on-device constraints.

Our main contributions are:

- We introduce a geometry-prior construction operator \mathcal{G} that provides compact yet reliable geometric inputs for on-device 3DGS, reducing the dependence on heavy-weight reconstruction and costly training-time densification.
- We propose a prior-conditioned Gaussian parameterization operator \mathcal{I} that improves initialization quality and optimization conditioning, enabling stable convergence under a strict on-device iteration budget.
- We develop a hardware-aligned splatting optimization operator \mathcal{T} that renders differentiable splatting practical on mobile GPUs, supporting accurate gradients and

stable updates within hardware memory and bandwidth constraints.

We empirically show that PocketGS satisfies strict on-device runtime and peak-memory budgets while achieving competitive perceptual quality compared with standard workstation 3DGS pipelines, on both publicly available benchmarks and our self-collected MobileScan dataset.

II. RELATED WORK

A. Novel View Synthesis

Novel view synthesis targets photorealistic rendering from unseen viewpoints [9], [10]. The field has progressed from implicit NeRF-style radiance fields [8], [11], [12] to more efficient explicit voxel/hash-grid representations [13]–[17], and further to 3DGS with rasterization-friendly Gaussians for fast training and rendering [1], [18], [19]. Despite advances [4], [20]–[26], most 3DGS pipelines still rely on offline SfM [27], [28] for pose and sparse geometry, whose high cost and incomplete coverage hinder practical on-device training in resource-constrained settings.

B. Mobile 3D Scanning

Mobile 3D scanning captures images on mobile devices and reconstructs real-world 3D structure, typically via visual-inertial odometry for pose estimation and multi-view stereo for geometry [29]–[32]. Systems such as ARKit and ARCore follow this pipeline [33]–[35] but are limited by point/mesh representations, whose sparse and noisy reconstructions lack the capacity for high-fidelity rendering [9], [10]. Meanwhile, novel view synthesis has shown superior modeling and rendering quality, opening new opportunities for mobile 3D scanning [1], [9]; however, existing efforts largely emphasize mobile rendering efficiency [36], [37], leaving on-device training underexplored.

III. THE POCKETGS PARADIGM

PocketGS enables on-device 3D Gaussian Splatting (3DGS) training under strict runtime and peak-memory constraints. Given a sequence of video frames $\{I_t\}_{t=1}^n$ and their corresponding coarse camera poses $\{\hat{T}_t\}_{t=1}^n$ obtained from mobile tracking systems (ARKit or ARCore), PocketGS comprises three tightly coupled operators. Specifically, the geometry operator \mathcal{G} refines the coarse poses $\{\hat{T}_t\}$ into accurate ones $\{T_t\}$, and extracts a dense point cloud P , which serves as a reliable geometric prior. The initialization operator \mathcal{I} maps P to a well-conditioned 3D Gaussian initialization Θ_0 . Finally, the training operator \mathcal{T} performs hardware-aligned differentiable rendering to optimize Θ_0 into the final Gaussian representation Θ^* . Formally, these operators are defined as: $\mathcal{G} : (\{I_t, \hat{T}_t\}) \mapsto (\{T_t\}, P)$, $\mathcal{I} : P \mapsto \Theta_0$, and $\mathcal{T} : (\Theta_0, \{I_t, T_t\}) \mapsto \Theta^*$.

A. Geometry Prior Construction under Resource Budgets

Prior 3DGS approaches rely on prolonged optimization with training-time densification to recover scenes from noisy and sparse point inputs. On mobile devices, this paradigm often yields unstable geometry recovery and substantial computational overhead, making it impractical under on-device

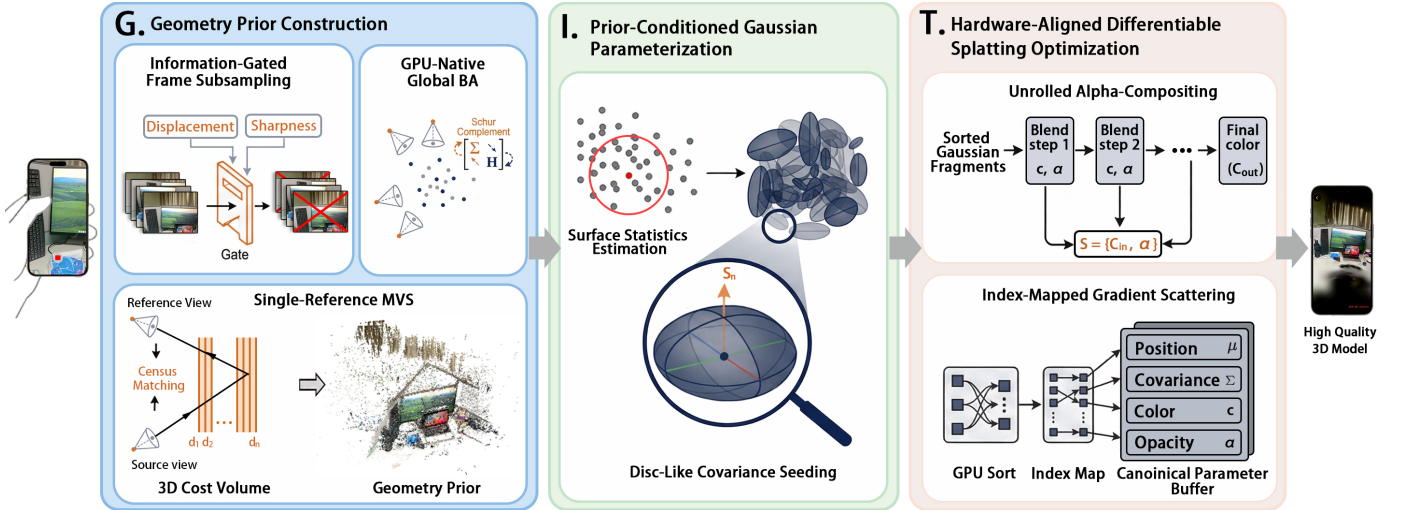


Fig. 2: **Overview of the PocketGS framework.** PocketGS tackles on-device 3DGS training through three coupled operators: (\mathcal{G}) Geometry Prior Construction employs an information-gated gate for frame selection, followed by GPU-native Schur-complement BA and single-reference MVS. The MVS module constructs a 3D cost volume by sampling depth hypotheses d_1, \dots, d_n via census matching to produce a dense geometric scaffold. (\mathcal{I}) Prior-Conditioned Parameterization seeds anisotropic Gaussians by estimating local surface statistics (normals s_n and scales) to front-load structure discovery via disc-like covariance seeding. (\mathcal{T}) Hardware-Aligned Splatting implements a mobile-native differentiable renderer using unrolled alpha-compositing ($S = id, C_{in}, \alpha$) and index-mapped gradient scattering to ensure stable backpropagation within tight mobile memory bounds of the canonical parameter buffer (μ, Σ, c, α).

constraints. We instead leverage the mobile capture $\{I_t, \hat{T}_t\}$ to build a dense, low-noise, and low-redundancy geometry prior by applying a geometry operator \mathcal{G} , which maps $(\{I_t, \hat{T}_t\})$ to refined poses $\{T_t\}$ and a compact geometric representation P . Conditioning the subsequent optimization on $(\{T_t\}, P)$ removes the need for training-time densification, resulting in more stable convergence and improved computational efficiency.

1) *Information-Gated Frame Subsampling*: Video frames captured during mobile scanning are often affected by motion blur, which degrades geometric reconstruction and undermines the photometric optimization of 3DGS. To mitigate this issue, we subsample the input sequence using an information-gated keyframe selection strategy based on viewpoint change and distance variation, retaining only sharp and high-utility frames while filtering out blurred and redundant ones.

Displacement Gate. We ensure sufficient parallax for robust triangulation by computing the camera displacement d between the current frame \mathbf{t}_{curr} and the last selected keyframe \mathbf{t}_{last} , $d = \|\mathbf{t}_{curr} - \mathbf{t}_{last}\|_2$. A frame is considered only if $d \geq \tau_d$, where $\tau_d = 0.05m$, suppressing redundant viewpoints while maintaining tracking stability.

Sharpness Heuristic. We reject frames degraded by motion or defocus blur using an efficient approximation of gradient energy. We estimate the sharpness score S by summing absolute luma differences over a sparsely sampled grid Ω :

$$S = \frac{1}{|\Omega|} \sum_{(x,y) \in \Omega} (|I(x+\Delta, y) - I(x, y)| + |I(x, y+\Delta) - I(x, y)|) \quad (1)$$

where Δ is the step size. This score correlates with high-frequency content and favors sharp frames.

Candidate Windowing. We select the locally optimal frame from a short temporal window (8 frames). A candidate replaces the current best only if $S_{new} > (1+r)S_{best}$, with $r = 0.05$. This commits the sharpest representative per viewpoint and bounds downstream optimization workload.

2) *GPU-Native Global BA as Mobile MAP Refinement*: Initial camera poses provided by mobile tracking systems (e.g., ARKit and ARCore) are often noisy, which degrades both geometric reconstruction and the photometric optimization of 3DGS. To address this issue, we perform GPU-native global BA on-device to refine poses, thereby providing accurate pose estimates for subsequent dense point recovery and 3DGS optimization.

The robustified reprojection objective for PocketGS:

$$\min_{\{\hat{T}_i\}, \{P_j\}} \sum_{i,j} \rho \left(\|\pi(\hat{T}_i, P_j) - \mathbf{p}_{ij}\|_{\Sigma_{ij}}^2 \right) \quad (2)$$

where π is the projection function, $\hat{T}_i \in SE(3)$ is the pose of camera i , $P_j \in \mathbb{R}^3$ is the 3D position of point j , $\mathbf{p}_{ij} \in \mathbb{R}^2$ is the observed 2D projection, and ρ is the robust Huber loss.

Scale-Aware Gauge Fixing. To resolve the 7-DoF ambiguity of monocular reconstruction, we fix the 6-DoF pose of the first keyframe and fix scale by constraining the translational component of the second keyframe along the dominant baseline axis, yielding a consistent metric frame.

GPU-Native Schur Complement. The BA bottleneck is solving the normal equations $\mathbf{H}\Delta = \mathbf{b}$, where $\mathbf{H} = \mathbf{J}^T \mathbf{J}$. We exploit the sparse block structure via a full GPU Schur complement. Partitioning parameters into camera pose (\mathbf{t}) and point (\mathbf{p}) blocks yields the reduced camera system:

$$(\mathbf{H}_{tt} - \mathbf{H}_{tp} \mathbf{H}_{pp}^{-1} \mathbf{H}_{pt}) \Delta_c = \mathbf{b}_t - \mathbf{H}_{tp} \mathbf{H}_{pp}^{-1} \mathbf{b}_p \quad (3)$$

Since \mathbf{H}_{pp} is block-diagonal with independent 3×3 blocks per point, \mathbf{H}_{pp}^{-1} is computed in parallel across points on the GPU. After solving for Δ_t , we recover Δ_p by back-substitution.

Iterative Geometric Refinement. BA is embedded in an iterative refinement loop. After each global step, we re-triangulate features using updated poses, filter points with high reprojection error or insufficient triangulation angles, and remove observations behind the camera. This purification reduces outliers and stabilizes dense reconstruction.

3) *Single-Reference Cost-Volume MVS*: Point clouds provided by mobile tracking systems are typically sparse, which necessitates costly densification during 3DGS training. To address this limitation, our lightweight MVS reconstructs a dense and geometry-faithful point cloud for Gaussian initialization, thereby reducing over-densification under mobile budgets.

Probabilistic Depth Range Estimation. Plane-sweep efficiency depends on depth range. For each target frame, we project sparse BA points and compute the 5% and 95% depth quantiles $q_{.05}$ and $q_{.95}$. We define the search range as $[q_{.05} \cdot 0.6, q_{.95} \cdot 1.6]$, focusing computation on the most probable volume.

Memory-Efficient Cost Volume. To minimize memory footprint, we construct the cost volume using only a single, optimally chosen reference frame. The reference maximizes

$$S_{ref} = \exp\left(-\frac{(b - b_{target})^2}{2\sigma_b^2}\right) \cdot \max\left(\frac{\alpha}{\alpha_{min}}, 1\right) \quad (4)$$

balancing baseline length b against a target baseline b_{target} and enforcing sufficient viewing angle α . The matching cost is computed using the Census Transform [38] for robustness to illumination changes. Depth is inferred via plane sweep [39] with Semi-Global Matching aggregation. We filter depth maps using a confidence threshold of 0.4 and fuse them into a dense point cloud, which serves as the geometric scaffold for \mathcal{I} .

B. Prior-Conditioned Gaussian Parameterization

Prior methods initialize points as isotropic Gaussians based solely on inter-point distances, resulting in arbitrary parameter initialization that requires unnecessary updates and consequently slow convergence. In contrast, we exploit point-cloud surface geometry P to estimate normals and initialize surface-aligned anisotropic Gaussians via an initialization operator \mathcal{I} , which maps P to the initial Gaussian parameters Θ_0 . This structure-consistent starting state $\Theta_0 = \mathcal{I}(P)$ improves conditioning and accelerates optimization under tight on-device budgets.

1) *Local Surface Statistics Estimation*: To extract geometric priors from the mobile capture, we estimate local surface statistics for each point \mathbf{p}_i in the dense MVS point cloud using a fixed-size KNN neighborhood ($K=16$). Let $\{\mathbf{p}_{i,k}\}_{k=1}^K$ denote the K nearest neighbors of \mathbf{p}_i , with centroid

$$\bar{\mathbf{p}}_i = \frac{1}{K} \sum_{k=1}^K \mathbf{p}_{i,k}. \quad (5)$$

We compute the local covariance as

$$\mathbf{C}_i = \frac{1}{K} \sum_{k=1}^K (\mathbf{p}_{i,k} - \bar{\mathbf{p}}_i)(\mathbf{p}_{i,k} - \bar{\mathbf{p}}_i)^\top. \quad (6)$$

The eigenvector of \mathbf{C}_i associated with its smallest eigenvalue provides an estimate of the local surface normal \mathbf{n}_i . This per-point, fixed- K procedure is embarrassingly parallel with bounded memory, making it well-suited for GPU execution under PocketGS’s mobile constraints.

C. Hardware-Aligned Differentiable Splatting Optimization

On mobile GPUs, on-device 3D Gaussian Splatting (3DGS) training is bandwidth-bound: fixed-function blending reveals only the final color, hiding the intermediate compositing states needed for backpropagation, while auxiliary-buffer clears incur heavy memory traffic. We therefore align optimization with the mobile pipeline by unrolling front-to-back compositing into an explicit differentiable operator and caching a compact forward replay trace. This defines a GPU-resident map $\mathcal{T}: (\Theta_0, \{I_t, T_t\}) \mapsto \Theta^*$ that delivers correct, stable gradients without framebuffer readbacks or backward-time reconstruction of per-pixel splat sequences.

1) *Unrolled Alpha-Compositing with Forward Replay Cache*: Mobile fixed-function blending returns only the final composited color, while 3DGS backpropagation requires the intermediate accumulator state at each compositing step. Moreover, the set and order of Gaussians contributing to a pixel are not accessible from the rendering pipeline, making a backward pass that replays the original per-pixel splat list infeasible or prohibitively expensive. We address this by (1) unrolling the front-to-back compositing into an explicit computation graph and (2) caching a compact forward replay trace per pixel for backward traversal.

a) *Explicit Computation Graph*: For depth-sorted visible Gaussians, we explicitly perform front-to-back compositing:

$$C_{out} = C_{in}(1 - \alpha) + \alpha c, \quad (7)$$

where C_{in} is the accumulator input and (α, c) are the opacity and color of the current Gaussian fragment. The backward pass follows the same unrolled chain:

$$\frac{\partial \mathcal{L}}{\partial C_{in}} = \frac{\partial \mathcal{L}}{\partial C_{out}}(1 - \alpha), \quad \frac{\partial \mathcal{L}}{\partial \alpha} = \left\langle \frac{\partial \mathcal{L}}{\partial C_{out}}, (c - C_{in}) \right\rangle, \quad (8)$$

where $\langle \cdot, \cdot \rangle$ denotes the per-channel inner product.

b) *Bandwidth-Efficient Forward Replay Cache*: To avoid backward-time reconstruction of per-pixel splat sequences, we record only the intermediates necessary to replay gradients:

$$S = \{\text{id}, C_{in}, \alpha\}, \quad (9)$$

where id is the (sorted) splat identifier used to scatter gradients back to canonical parameter buffers. A per-pixel counter $\text{count}(u)$ stores the number of valid cached entries for pixel u . Each iteration resets only the $O(WH)$ counters, rather than clearing the full $O(WHK_{\max})$ cache. During backpropagation, we traverse only

$$k \in [0, \text{count}(u) - 1],$$

treating stale cache entries beyond $\text{count}(u)$ as invalid, thereby eliminating bandwidth-heavy full-cache clears while preserving gradient correctness.

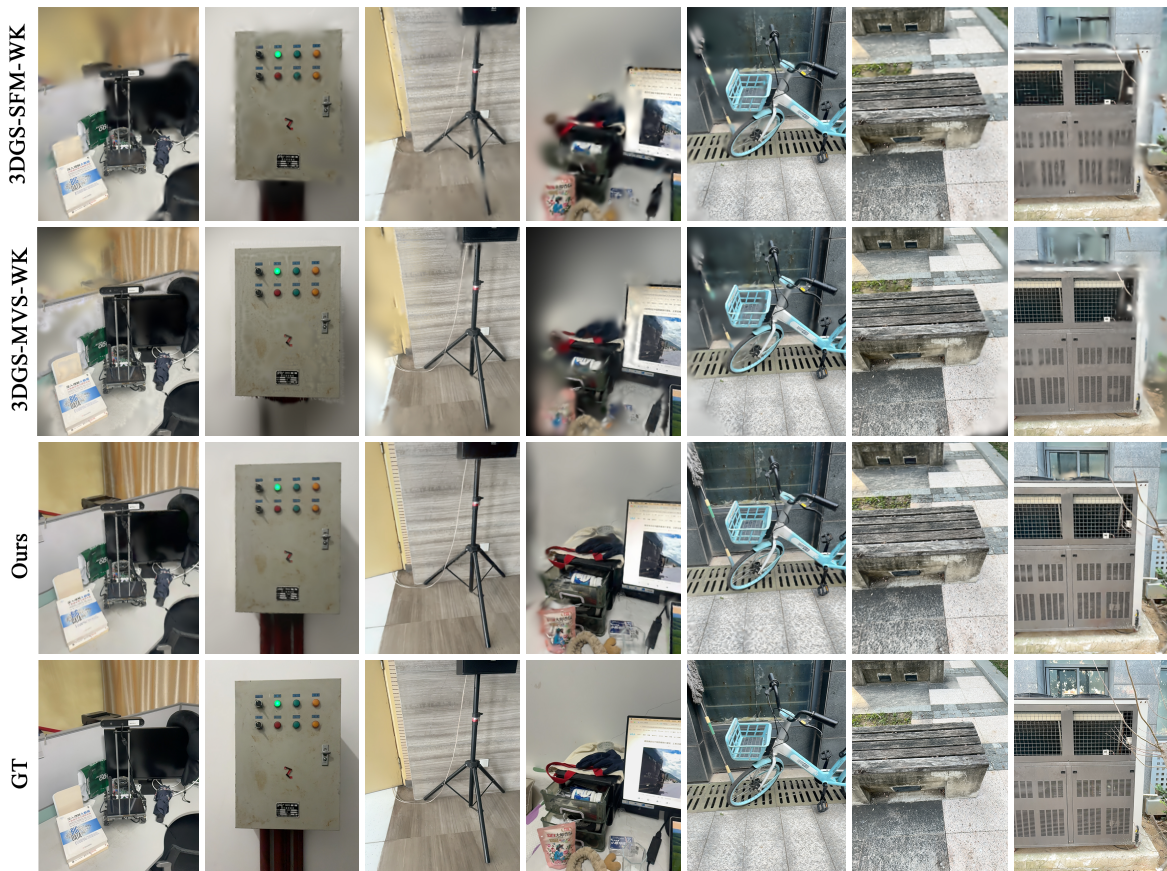


Fig. 3: Qualitative comparison on our MobileScan dataset. PocketGS (Ours) consistently recovers sharper textures and finer details compared to baselines. Notably, 3DGS-MVS-WK suffers from artifacts despite its high-density prior, as the over-concentrated initial points impede effective Gaussian redistribution within a limited iteration budget. Our method avoids this bottleneck through prior-conditioned initialization, achieving superior structural fidelity (e.g., bicycle spokes) that closely matches the ground truth (GT).

Method	LLFF					NeRF-Synthetic					MobileScan				
	PSNR \uparrow	SSIM \uparrow	LPIPS \downarrow	Time \downarrow (s)	Count	PSNR \uparrow	SSIM \uparrow	LPIPS \downarrow	Time \downarrow (s)	Count	PSNR \uparrow	SSIM \uparrow	LPIPS \downarrow	Time \downarrow (s)	Count
3DGS-SFM-WK	21.01	0.641	0.405	108.0	18k	21.75	0.800	0.243	83.7	12k	21.16	0.687	0.398	112.8	23k
3DGS-MVS-WK	19.53	0.637	0.387	313.1	40k	24.47	0.887	0.128	532.1	50k	20.85	0.781	0.281	534.5	165k
PocketGS (Ours)	23.54	0.791	0.222	105.4	33k	24.32	0.858	0.144	101.4	47k	23.67	0.791	0.225	255.2	168k

TABLE I: **Average Metrics Across Datasets.** Dataset-level averages on LLFF, NeRF Synthetic, and our MobileScan mobile-native dataset. Higher is better for PSNR/SSIM, and lower is better for LPIPS/Time. Best results are in **bold**.

2) *Index-Mapped Gradient Scattering:* Maintaining optimizer consistency during depth-sorted rendering typically requires physically reordering parameter buffers, which incurs heavy data movement and can misalign optimizer states. We resolve this by decoupling the *sorted view* used for rendering/backprop from the *canonical layout* used for parameter storage and optimizer moments. A GPU-based sort produces a permutation π that maps each sorted index i to its canonical index $\pi(i)$. The renderer and backward kernels operate on the sorted view, while gradients are scattered back to canonical buffers:

$$\nabla\theta_{\pi(i)} += g_i, \quad (10)$$

ensuring that Adam optimizer states (stored in canonical order) remain aligned with their respective parameters, without CPU intervention or redundant memory copies.

IV. EXPERIMENTS

A. Experimental Setup

1) *Implementation Details and Experimental Settings:* We implement PocketGS as a fully on-device system and evaluate it on an iPhone 15 (Apple A16). The entire process was written in Swift and accelerated by using the Apple Metal API to take advantage of the mobile GPU execution stack. Unless otherwise stated, all methods are evaluated under identical image resolution, color space, and metric implementations.

To reflect realistic mobile constraints, we use a fixed training budget for all methods. In particular, we optimize each model for a constant number of iterations (500 iterations) at a fixed view rendering resolution.

2) *Baselines:* We compare against two workstation baselines that follow the standard two-stage paradigm: (i) reconstruct camera poses and a point-cloud prior, and (ii) train

a standard 3D Gaussian Splatting (3DGS) model initialized from the reconstructed prior. All workstation experiments are conducted on a machine equipped with $2\times$ NVIDIA RTX 3090 GPUs and an Intel Core i9-class CPU. For both baselines, point-cloud reconstruction is performed using COLMAP [28].

a) 3DGS-SfM-WK: We adopt the standard COLMAP-based Structure-from-Motion (SfM) pipeline on a workstation to estimate camera extrinsic/intrinsic parameters and reconstruct a sparse point cloud. This sparse geometric prior is then used to initialize and train a vanilla 3D Gaussian Splatting (3DGS) model, adhering to the original 3DGS training protocol.

b) 3DGS-MVS-WK: For this workstation-based baseline, we leverage the standard COLMAP Multi-View Stereo (MVS) workflow to generate a dense point cloud as the geometric prior. Subsequently, a vanilla 3DGS model is initialized with this dense point cloud and trained following the default 3DGS optimization workflow.

We choose these two baselines because they (1) represent the standard reconstruction-first 3DGS pipeline, (2) span sparse SfM versus dense but costly MVS priors to separate prior quality from reconstruction overhead under matched budgets, and (3) provide a workstation reference that reflects PocketGS’s goal: competitive quality under strict on-device constraints without heavy offline reconstruction.

3) Datasets and Metrics:

a) Datasets.: We evaluate on three representative datasets spanning synthetic and real captures: NeRF-Synthetic [8], LLFF [40], and MobileScan. NeRF-Synthetic provides object-centric synthetic scenes with accurate poses; LLFF consists of real forward-facing captures exhibiting real-world degradations; and MobileScan is our Phone-captured dataset designed to reflect mobile imaging characteristics, including motion blur, defocus, and exposure variation. For MobileScan, we use ARKit-provided intrinsics, poses, and sparse structure to emulate practical on-device inputs, enabling evaluation under noisy geometric priors and limited compute budgets. More details are in the supplement.

b) Metrics.: We report standard novel-view synthesis metrics, including PSNR (dB, \uparrow), SSIM (\uparrow), and LPIPS (\downarrow). We additionally report end-to-end runtime to capture practical deployability. Specifically, we define the total runtime as

$$T_{\text{total}} = T_{\text{geom}} + T_{\text{train}}, \quad (11)$$

where T_{geom} includes geometry and pose acquisition as well as associated optimization, and T_{train} denotes the 3DGS optimization time. For fair comparison, all methods are evaluated under the same training budget and at the same rendering resolution. Finally, we report Count (the number of Gaussians) to characterize the trade-off between representation capacity and computational efficiency.

B. Main Results: Quality and Efficiency Comparison

Table I summarizes averages under a strict, matched optimization budget. Across all datasets, PocketGS consistently delivers a strong quality–efficiency trade-off while maintaining *compact or comparable* Gaussian counts, indicating better representation efficiency.

a) LLFF Dataset.: LLFF stresses forward-facing captures and view extrapolation, where imperfect geometry can destabilize optimization. PocketGS achieves the best overall quality while remaining fast. Notably, 3DGS-MVS-WK performs poorly despite a larger Count, suggesting that a generic dense prior does not ensure good convergence in this regime. In contrast, PocketGS attains higher quality with fewer Gaussians, indicating better representation efficiency and conditioning under the same iteration budget.

Fig. 4 shows PocketGS better preserves fine, high-frequency geometry structures (e.g., *leaves in Fern, petals in Flower*), with fewer floating artifacts and cleaner boundaries. This is consistent with our refined geometry prior (\mathcal{G}) and robust anisotropic initialization (\mathcal{I}), which improve pose/structure consistency and reduce Gaussian drift during optimization.

b) NeRF-Synthetic Dataset.: On the geometry-clean NeRF Synthetic dataset, 3DGS-MVS-WK achieves the best metrics, as its dense prior matches the ground-truth geometry. PocketGS remains competitive (PSNR 24.32 vs. 24.47) while being $\sim 5.2\times$ faster in end-to-end runtime T_{total} (101.4s vs. 532.1s), mainly by avoiding the costly offline dense reconstruction in 3DGS-MVS-WK. With a similar Count (47k vs. 50k), this speedup reflects a more streamlined pipeline and hardware-aligned splatting rather than reduced capacity.

Fig. 5 shows PocketGS preserves high-fidelity appearance and clean edges under the same budget, closely matching 3DGS-MVS-WK, demonstrating that PocketGS can substantially reduce capture-to-reconstruction latency without sacrificing quality when geometry is well-conditioned.

c) MobileScan Dataset.: On the challenging MobileScan dataset, PocketGS consistently outperforms 3DGS-SfM-WK, indicating that our mobile-native prior construction mitigates instability from sparse/noisy mobile inputs. Compared to 3DGS-MVS-WK, PocketGS achieves better perceptual quality (LPIPS 0.225 vs. 0.281) with much lower end-to-end time (255.2s vs. 534.5s), suggesting that heavyweight offline dense reconstruction is inefficient for mobile deployment. Notably, although PocketGS and 3DGS-MVS-WK converge to similar primitives, PocketGS renders more faithfully, implying improved *placement* rather than merely the *quantity* of Gaussians.

Fig. 3 shows that 3DGS-SfM-WK often yields blurry textures and structural collapse, consistent with its low Count (23k) and unreliable geometry. While 3DGS-MVS-WK starts from a dense prior, it still exhibits artifacts when Gaussians are overly concentrated; under a limited optimization budget, it cannot sufficiently re-balance spatial coverage, leading to ghosting and local inconsistency. PocketGS avoids this by surface-aligned, spatially balanced anisotropic initialization, producing sharper textures and higher structural fidelity closer to GT.

d) On-device Rendering and Deployment Perspective.: Beyond metrics, Fig. 6 demonstrates real-time rendering screenshots produced on an iPhone 15 across MobileScan, LLFF, and NeRF Synthetic scenes. The consistently sharp details across diverse scales and capture conditions indicate robust generalization in practical deployment. PocketGS maintains high perceptual quality under mobile memory and

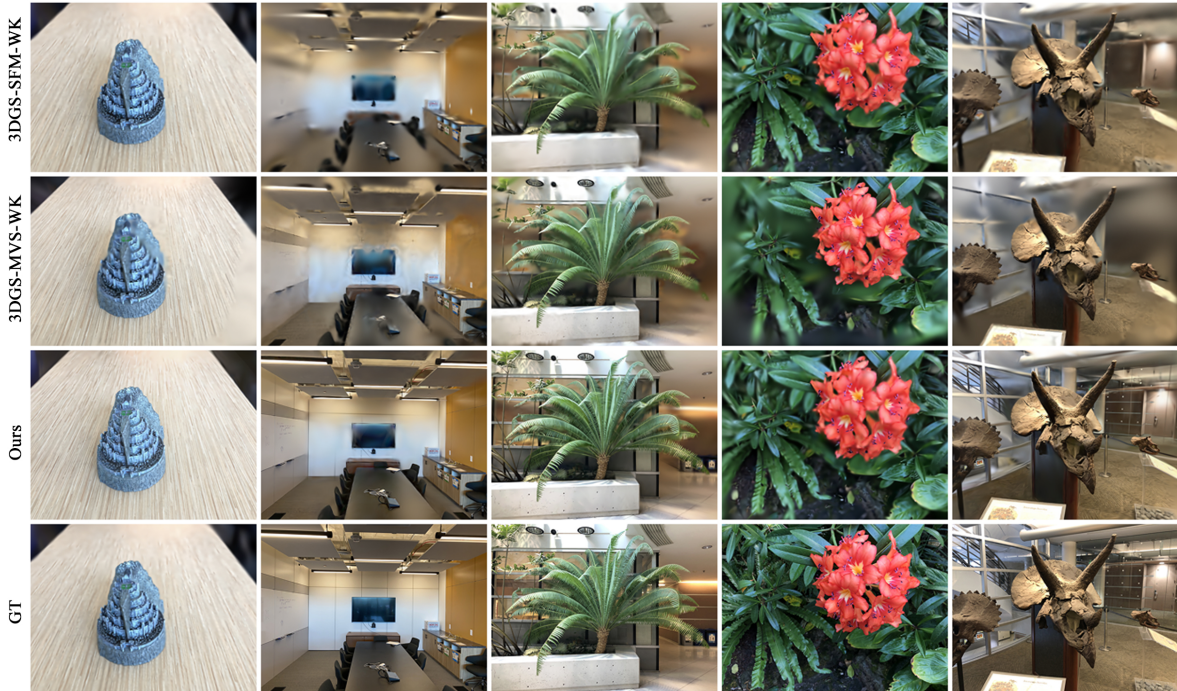


Fig. 4: **Qualitative comparison on the LLFF dataset.** Our method produces much sharper textures and more accurate thin structures (e.g., the leaves in Fern and the petals in Flower), closely matching the ground truth (GT).

bandwidth constraints by avoiding unnecessary densification while preserving critical structures.

C. Memory Footprint

We profile peak memory usage on MobileScan to quantify the practicality of our on-device pipeline. Following our end-to-end definition, we report memory for two stages: (i) geometry prior construction and (ii) full 3DGS training. In all measurements, peak memory is recorded as the maximum resident memory observed during execution, and the statistics are aggregated over all MobileScan scenes.

Full 3DGS training reaches an average peak of 2.21 GB (range: 1.82–2.65 GB), reflecting the combined cost of storing the Gaussian parameters, intermediate buffers for rasterization, and optimizer states. Geometry prior construction peaks at 1.53 GB on average (range: 1.19–2.22 GB), dominated by temporary buffers used for feature processing, correspondence aggregation, and incremental updates of the prior representation. Importantly, across all scenes the peak memory remains below 3 GB, which fits within the on-device budget and leaves practical headroom for commodity smartphones to accommodate system overhead and concurrent background processes. We provide per-scene peak memory breakdowns for both stages in the supplemental material.

D. Ablation Study

We conduct an ablation study on the MobileScan dataset to quantify the contribution of each core component of PocketGS. The study follows the same experiment setup, and we summarize dataset averages in Table II.

Information-Gated Frame Subsampling. Removing information-gated subsampling admits motion/defocus-degraded frames, corrupting the geometry prior and cascading

Variant	PSNR \uparrow	SSIM \uparrow	LPIPS \downarrow	Time \downarrow (s)
PocketGS (Full)	23.67	0.791	0.225	255.2
w/o Initialization (\mathcal{I})	22.49	0.7696	0.253	319.5
w/o Global BA	23.45	0.7517	0.232	251.1
w/o MVS	21.07	0.6461	0.414	124.8

TABLE II: **Ablation Summary on MobileScan Dataset (Averages).**

into poorer initialization and blurrier reconstructions; the full pipeline better preserves sharp details (fig. 7).

GPU-native Global BA. Disabling Global BA yields a clear SSIM drop (from 0.791 to 0.7517) with minor PSNR/LPIPS changes, indicating reduced global coherence and pose consistency, while incurring negligible runtime overhead (251.1s vs. 255.2s).

Single-Reference Cost-Volume MVS. Removing lightweight MVS causes the largest quality degradation (PSNR 21.07, SSIM 0.6461, LPIPS 0.4137), showing dense geometric support largely sets the quality ceiling; although runtime drops to 124.8s, quality falls to the level of 3DGS-SFM-WK.

Prior-Conditioned Gaussian Parameterization. Removing \mathcal{I} degrades all metrics (PSNR 23.67 \rightarrow 22.49) and increases end-to-end time (255.2s \rightarrow 319.5s), suggesting prior-conditioned initialization is critical for convergence efficiency under a limited iteration budget.

V. CONCLUSION

In this paper, we present **PocketGS**, a fully on-device training framework for 3D Gaussian Splatting that targets the practical constraints of mobile devices. PocketGS is built upon three co-designed operators: (**G**) geometry-prior construction

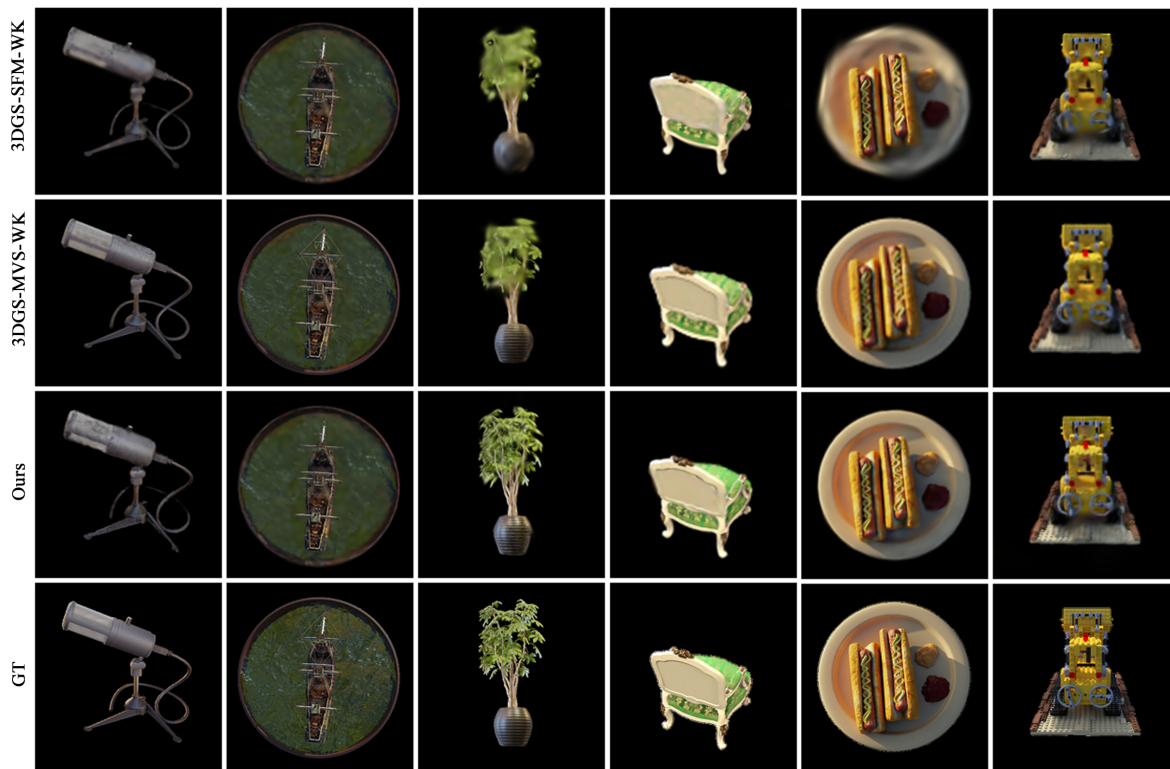


Fig. 5: **Qualitative comparison on the NeRF Synthetic dataset.** In these object-centric synthetic scenes, our method produces high-fidelity results.

to provide compact and reliable geometric guidance, **(I)** prior-conditioned Gaussian parameterization to improve initialization and optimization under iteration-limited budgets, and **(T)** hardware-aligned splatting optimization to ensure efficient and stable differentiable splatting on mobile GPUs. Extensive experiments on public benchmarks and our MobileScan dataset show that PocketGS achieves strong perceptual quality while meeting smartphone budgets, e.g., **approximately 4-minute** end-to-end training with **< 3 GB** peak memory on iPhone 15. These results indicate that high-fidelity 3D reconstruction and mobile 3D content creation can be made practical on commodity devices.

REFERENCES

- [1] B. Kerbl, G. Kopanas, T. Leimkühler, and G. Drettakis, “3d gaussian splatting for real-time radiance field rendering,” *ACM Trans. Graph.*, vol. 42, no. 4, 2023.
- [2] J. Gao, C. Gu, Y. Lin, Z. Li, H. Zhu, X. Cao, L. Zhang, and Y. Yao, “Relightable 3D Gaussians: Realistic Point Cloud Relighting with BRDF Decomposition and Ray Tracing,” in *ECCV*, 2024.
- [3] Z. Liang, Q. Zhang, Y. Feng, Y. Shan, and K. Jia, “GS-IR: 3D Gaussian Splatting for Inverse Rendering,” in *CVPR*, 2024.
- [4] B. Huang, Z. Yu, A. Chen, A. Geiger, and S. Gao, “2d gaussian splatting for geometrically accurate radiance fields,” *ACM SIGGRAPH 2024 Conference Proceedings*, 2024.
- [5] Z. Yu, T. Sattler, and A. Geiger, “Gaussian Opacity Fields: Efficient Adaptive Surface Reconstruction in Unbounded Scenes,” *ACM TOG*, vol. 43, no. 6, pp. 1–13, 2024.
- [6] A. Escontrela, J. Kerr, A. Allshire, J. Frey, R. Duan, C. Sferrazza, and P. Abbeel, “GaussGym: An Open-Source Real-to-Sim Framework for Learning Locomotion from Pixels,” *arXiv preprint arXiv:2510.15352*, 2025.
- [7] M. Zhang, K. Zhang, and Y. Li, “Dynamic 3D Gaussian Tracking for Graph-Based Neural Dynamics Modeling,” in *CoRL*, 2025.
- [8] B. Mildenhall, P. P. Srinivasan, M. Tancik, J. T. Barron, R. Ramamoorthi, and R. Ng, “Nerf: Representing scenes as neural radiance fields for view synthesis,” *Communications of the ACM*, vol. 65, no. 1, pp. 99–106, 2021.
- [9] A. Tewari, J. Thies, B. Mildenhall, P. Srinivasan, E. Tretschk, W. Yifan, C. Lassner, V. Sitzmann, R. Martin-Brualla, S. Lombardi *et al.*, “Advances in neural rendering,” in *Computer Graphics Forum*, vol. 41, no. 2. Wiley Online Library, 2022, pp. 703–735.
- [10] K. Gao, Y. Gao, H. He, D. Lu, L. Xu, and J. Li, “Nerf: Neural radiance field in 3d vision, a comprehensive review,” *arXiv preprint arXiv:2210.00379*, 2022.
- [11] J. T. Barron, B. Mildenhall, M. Tancik, P. Hedman, R. Martin-Brualla, and P. P. Srinivasan, “Mip-NeRF: A Multiscale Representation for Anti-Aliasing Neural Radiance Fields,” in *ICCV*, 2021.
- [12] J. T. Barron, B. Mildenhall, M. Tancik, P. P. Srinivasan, X. Han, and R. Martin-Brualla, “Mipnerf 360: Unbounded anti-aliased neural radiance fields,” in *IEEE/CVF Conference on Computer Vision and Pattern Recognition (CVPR)*, 2022.
- [13] S. Fridovich-Keil, A. Yu, M. Tancik, Q. Chen, B. Recht, and A. Kanazawa, “Plenoxels: Radiance fields without neural networks,” in *Proceedings of the IEEE/CVF conference on computer vision and pattern recognition*, 2022, pp. 5501–5510.
- [14] C. Sun, M. Sun, and H.-T. Chen, “Direct Voxel Grid Optimization: Super-Fast Convergence for Radiance Fields Reconstruction,” in *CVPR*, 2022.
- [15] T. Müller, A. Evans, C. Schied, and A. Keller, “Instant neural graphics primitives with a multiresolution hash encoding,” *ACM Trans. Graph.*, vol. 41, no. 4, 2022.
- [16] J. T. Barron, B. Mildenhall, D. Verbin, P. P. Srinivasan, and P. Hedman, “Zip-NeRF: Anti-Aliased Grid-Based Neural Radiance Fields,” in *ICCV*, 2023.
- [17] W. Guo, B. Wang, and L. Chen, “Neuv-slam: Fast neural multiresolution voxel optimization for rgbd dense slam,” *IEEE Transactions on Multimedia*, 2025.
- [18] G. Fang and B. Wang, “Mini-splatting: Representing scenes with a constrained number of gaussians,” in *European Conference on Computer Vision*. Springer, 2024, pp. 165–181.
- [19] —, “Mini-splatting2: Building 360 scenes within minutes via aggressive gaussian densification,” *arXiv preprint arXiv:2411.12788*, 2024.

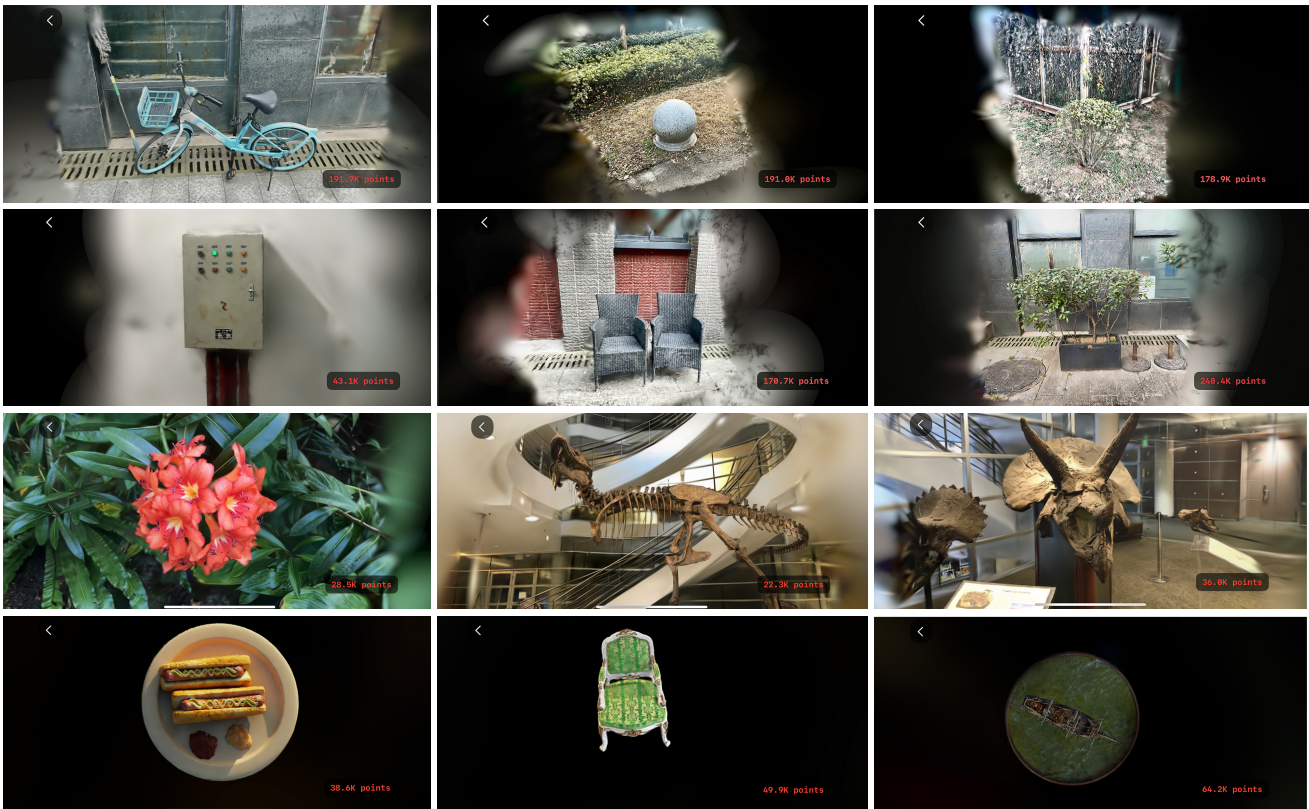


Fig. 6: **Qualitative results on a mobile device across diverse datasets.** We showcase real-time rendering screenshots from an iPhone 15, covering our self-collected scenes (rows 1-2), LLFF (row 3), and NeRF Synthetic (row 4). PocketGS consistently achieves high-fidelity reconstruction and sharp details across varying scene scales and capture conditions. The red labels indicate optimized point counts, demonstrating our method’s representation efficiency and robust generalization for practical on-device deployment.

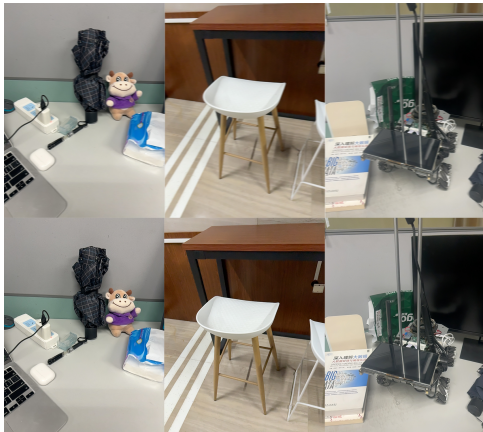


Fig. 7: Ablation of information-gated frame subsampling. Our method can obtain better details information.

[20] Z. Peng, T. Shao, Y. Liu, J. Zhou, Y. Yang, J. Wang, and K. Zhou, “Rtg-slam: Real-time 3d reconstruction at scale using gaussian splatting,” *ACM SIGGRAPH 2024 Conference Proceedings*, 2024.

[21] C. Yan, D. Qu, D. Xu, B. Zhao, Z. Wang, D. Wang, and X. Li, “Gs-slam: Dense visual slam with 3d gaussian splatting,” in *Proceedings of the IEEE/CVF Conference on Computer Vision and Pattern Recognition (CVPR)*, 2024.

[22] G. Wenzhi, B. Haiyang, M. Yuanqu, L. Jia, and C. Lijun, “Fvlocnerf: Fast vision-only localization within neural radiation field,” in *2023 IEEE/RSJ International Conference on Intelligent Robots and Systems (IROS)*. IEEE, 2023, pp. 3329–3334.

[23] D. Chen, H. Li, W. Ye, Y. Wang, W. Xie, S. Zhai, N. Wang, H. Liu,

H. Bao, and G. Zhang, “PGSR: Planar-based Gaussian Splatting for Efficient and High-Fidelity Surface Reconstruction,” *IEEE TVCG*, 2024.

[24] L. Höllein, A. Božič, M. Zollhöfer, and M. Nießner, “3dgs-lm: Faster gaussian-splatting optimization with levenberg-marquardt,” in *Proceedings of the IEEE/CVF International Conference on Computer Vision*, 2025, pp. 26 740–26 750.

[25] Y. Chen, J. Jiang, K. Jiang, X. Tang, Z. Li, X. Liu, and Y. Nie, “Dashgaussian: Optimizing 3d gaussian splatting in 200 seconds,” in *Proceedings of the Computer Vision and Pattern Recognition Conference*, 2025, pp. 11 146–11 155.

[26] G. Fang and B. Wang, “Efficient Scene Modeling Via Structure-Aware and Region-Prioritized 3D Gaussians,” *IEEE TPAMI*, 2025.

[27] B. Triggs, P. F. McLauchlan, R. I. Hartley, and A. W. Fitzgibbon, “Bundle adjustment — a modern synthesis,” in *Vision Algorithms: Theory and Practice*. Springer, 1999.

[28] J. L. Schönberger and J.-M. Frahm, “Structure-from-motion revisited,” in *Proceedings of the IEEE Conference on Computer Vision and Pattern Recognition (CVPR)*, 2016.

[29] Q. Picard, S. Chevobbe, M. Darouich, and J.-Y. Didier, “A survey on real-time 3d scene reconstruction with slam methods in embedded systems,” *arXiv preprint arXiv:2309.05349*, 2023.

[30] T. Qin, P. Li, and S. Shen, “Vins-mono: A robust and versatile monocular visual-inertial state estimator,” *IEEE Transactions on Robotics*, vol. 34, no. 4, pp. 1004–1020, 2018.

[31] Y. Furukawa and J. Ponce, “Accurate, dense, and robust multiview stereopsis,” *IEEE transactions on pattern analysis and machine intelligence*, vol. 32, no. 8, pp. 1362–1376, 2009.

[32] Y. Yao, Z. Luo, S. Li, T. Fang, and L. Quan, “Mvsnet: Depth inference for unstructured multi-view stereo,” in *European Conference on Computer Vision (ECCV)*, 2018.

[33] P. Kim, J. Kim, M. Song, Y. Lee, M. Jung, and H.-G. Kim, “A benchmark comparison of four off-the-shelf proprietary visual-inertial odometry systems,” *Sensors*, vol. 22, no. 24, p. 9873, 2022.

- [34] T. Feigl, A. Porada, S. Steiner, C. Löffler, C. Mutschler, and M. Philippsen, "Localization limitations of arcort, arkit, and hololens in dynamic large-scale industry environments." in *VISIGRAPP (I: GRAPP)*, 2020, pp. 307–318.
- [35] R. Mur-Artal and J. D. Tardós, "Orb-slam2: An open-source slam system for monocular, stereo, and rgb-d cameras," *IEEE transactions on robotics*, vol. 33, no. 5, pp. 1255–1262, 2017.
- [36] Z. Chen, T. Funkhouser, P. Hedman, and A. Tagliasacchi, "Mobilenerf: Exploiting the polygon rasterization pipeline for efficient neural field rendering on mobile architectures," in *Proceedings of the IEEE/CVF Conference on Computer Vision and Pattern Recognition*, 2023, pp. 16 569–16 578.
- [37] S. Rojas, J. Zarzar, J. C. Pérez, J. Sanchez-Riera, A. Rodríguez, F. Segu, and F. Moreno-Noguer, "Re-rend: Real-time rendering of nerfs across devices," in *Proceedings of the IEEE/CVF International Conference on Computer Vision (ICCV)*, 2023.
- [38] W. S. Fife and J. K. Archibald, "Improved census transforms for resource-optimized stereo vision," *IEEE Transactions on Circuits and Systems for Video Technology*, vol. 23, no. 1, pp. 60–73, 2012.
- [39] X. Yang, L. Zhou, H. Jiang, Z. Tang, Y. Wang, H. Bao, and G. Zhang, "Mobile3drecon: Real-time monocular 3d reconstruction on a mobile phone," *IEEE Transactions on Visualization and Computer Graphics*, vol. 26, no. 12, pp. 3446–3456, 2020.
- [40] B. Mildenhall, P. P. Srinivasan, R. Ortiz-Cayon, N. K. Kalantari, R. Ramamoorthi, R. Ng, and A. Kar, "Local light field fusion: Practical view synthesis with prescriptive sampling guidelines," *ACM Transactions on Graphics (ToG)*, vol. 38, no. 4, pp. 1–14, 2019.

APPENDIX

In this section, we provide additional details regarding the three core operators of PocketGS: Geometry Prior Construction (\mathcal{G}), Prior-Conditioned Parameterization (\mathcal{I}), and Hardware-Aligned Splatting (\mathcal{T}).

A. Geometry Prior Construction (\mathcal{G})

a) Information-Gated Frame Selection: To ensure high-quality input under a limited time budget, we implement a real-time frame selection mechanism during the capture phase. We utilize a displacement gate $\tau = 0.05\text{m}$ to filter redundant frames. For frames passing the displacement gate, we employ a candidate window mechanism (maximum 8 frames or 0.25s) to select the sharpest frame. Sharpness is computed by calculating the gradient energy on a sparse 160×160 grid of the luma plane, prioritizing frames with higher high-frequency content to mitigate motion blur.

b) GPU-Native Global Bundle Adjustment: Our global BA optimizes both camera poses and 3D point coordinates. We establish geometric constraints by extracting ORB/FAST features with BRIEF descriptors, accelerated via Metal. Feature matching is performed using Hamming distance with ratio tests and cross-checks. We implement an iterative refinement process (typically 3 rounds) that includes re-triangulation and outlier filtering based on reprojection error and triangulation angles. The optimization uses a Levenberg-Marquardt (LM) solver with Schur complement, fully resident on the GPU. To fix the gauge, we anchor the first frame's 6DoF and the scale of the baseline between the first two frames.

c) Lightweight Single-Reference MVS: For dense reconstruction, we estimate per-frame depth maps using a plane-sweep algorithm. To optimize memory, we select the top-3 reference frames based on baseline distance and viewing angle but only utilize the best reference frame for cost volume construction. The depth search range is dynamically estimated

using the 5%–95% quantiles of sparse point depths. We use Census transform for robust matching and Semi-Global Matching (SGM) for cost aggregation. The final dense point cloud is generated by back-projecting pixels with confidence ≥ 0.4 and depth within 0.05m to 5.0m.

B. Prior-Conditioned Parameterization (\mathcal{I})

We initialize Gaussian primitives by leveraging the local surface statistics derived from the MVS point cloud. For each point, we estimate the local surface normal using PCA on its $k = 16$ nearest neighbors. The scale parameters are initialized based on the average distance to the $k = 3$ nearest neighbors. To seed anisotropic Gaussians, we set the scale along the normal direction to $0.3 \times$ the tangential scales, effectively creating disc-like primitives that better align with the scene geometry.

C. Hardware-Aligned Splatting (\mathcal{T})

Our differentiable renderer is tailored for Tile-Based Deferred Rendering (TBDR) GPUs. We implement a multi-stage pipeline where alpha compositing is manually unrolled within the fragment shader. This allows us to cache intermediate states in tile memory, avoiding expensive global memory traffic. For backpropagation, we use index-mapped gradient scattering to ensure that gradients are correctly accumulated into the canonical parameter buffer despite the depth-sorted rendering order.

To demonstrate the feasibility and practicality of our end-to-end on-device training system, we developed a dedicated mobile application, PocketGS, which integrates the entire pipeline from data capture to 3DGS training. The application is built on the Metal framework for high-performance GPU computation.

The application workflow, as illustrated in Figure 8, is designed to be intuitive and efficient:

- **Main Menu (Fig. 8a):** Provides access to the core functionalities: Splat Capture (data acquisition), View Point Cloud and View 3DGS (visualization), Splat Training (optimization), Import Dataset, and Process Capture (geometry prior construction).
- **Splat Capture (Fig. 8b):** A guided capture interface that uses the information-gated frame selection mechanism to ensure high-quality input images (e.g., 50 frames) are collected in real-time, minimizing motion blur and redundancy.
- **Process Capture (Fig. 8c):** This module manages captured scenes and executes the Geometry Prior Construction (\mathcal{G}) operator, including the GPU-native BA and lightweight MVS, to generate the initial PLY point cloud. Users can manage captured data and trigger the processing step.
- **Splat Training (Fig. 8d):** This interface allows users to configure and initiate the on-device 3DGS training. Key features include selecting the input PLY file, choosing between Original Pose (ARKit pose) and Optimized Pose (BA-refined pose), and setting core hyperparameters (e.g., learning rates, iterations). The training process, which

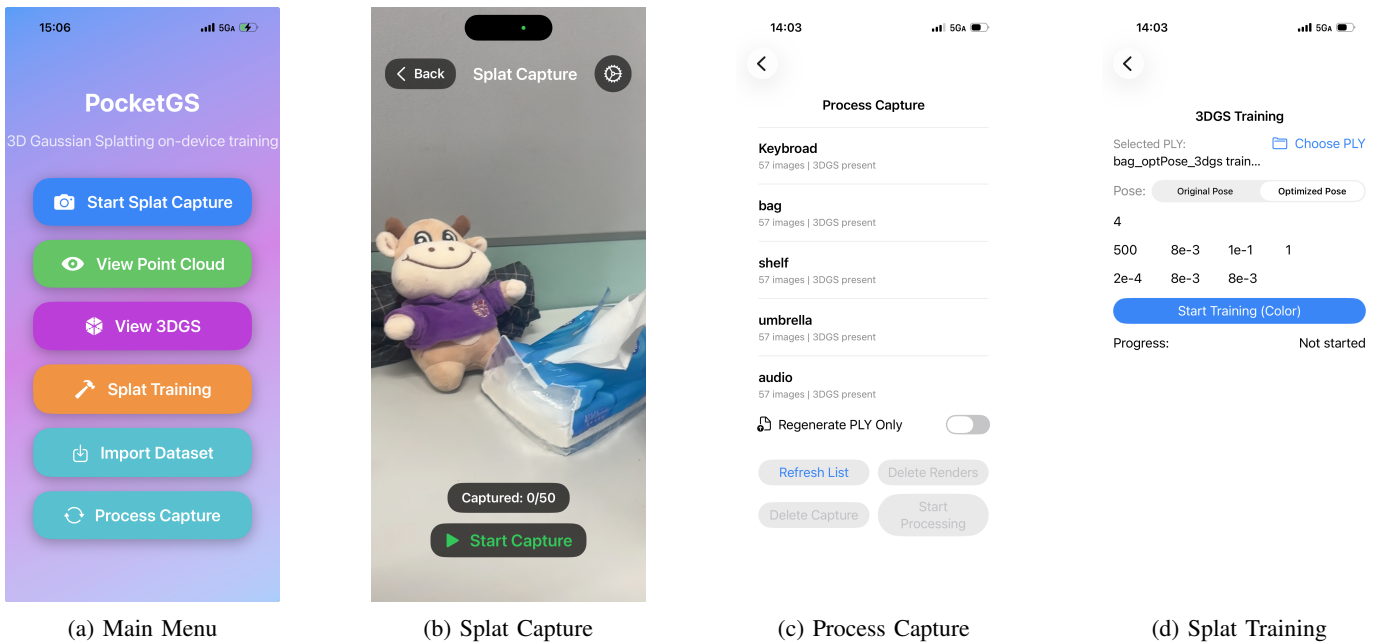


Fig. 8: Screenshots of the PocketGS mobile application, illustrating the end-to-end workflow.

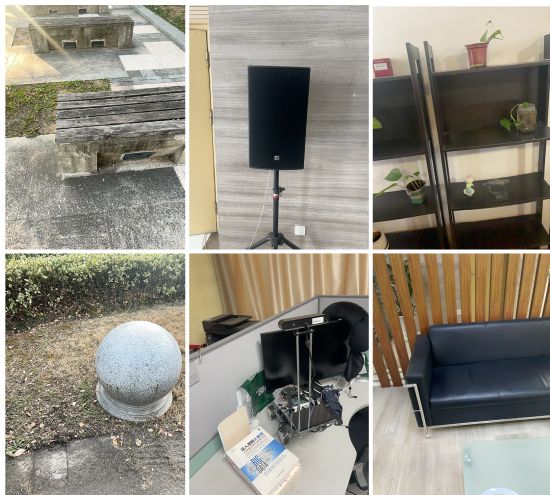


Fig. 9: The scenes on MobileScan Dataset.

implements the \mathcal{I} and \mathcal{T} operators, runs entirely on the mobile GPU, with progress displayed in real-time.

The PocketGS app serves as a concrete proof-of-concept, demonstrating that high-quality 3DGS training can be achieved end-to-end on a commodity mobile device within minutes.

The MobileScan dataset consists of 16 diverse indoor and outdoor scenes captured using iPhone 15. The statistics of the collected scenes are summarized in Table III. Each scene includes 50 high-resolution images with corresponding ARKit poses and sparse point clouds as baselines, as shown on 9.

Category	Scenes	Environment
Furniture	Sofa, Table, Desk, Shelf	Indoor
Objects	Robot, Audio, Printer, Bag, Elxbox, audio.	Indoor
Outdoor	Pier, Shrub, Bench, Bike, Transformer, Chair, Flowerpot	Outdoor

TABLE III: Statistics of the MobileScan Dataset.

The dataset covers various challenging scenarios, including:

- **Textureless Surfaces:** Large uniform areas like the "Sofa" and "Desk" scenes.
- **Complex Geometry:** Intricate structures in the "Transformer" and "Shrub" scenes.
- **Varying Lighting:** Outdoor scenes like "Pier" with natural lighting transitions.

We provide per-scene metrics for our MobileScan dataset, NeRF Synthetic dataset, and LLFF dataset. These tables serve as the full, unaggregated data supporting the main paper's claims on performance metrics (PSNR, SSIM, LPIPS) and efficiency (Time, Count).

D. MobileScan Dataset Comparison

The detailed per-scene quantitative results on our d MobileScan dataset are presented in Table IV. PocketGS consistently outperforms 3DGS-SFM-WK and 3DGS-MVS-WK in terms of perceptual quality (LPIPS) while maintaining a significantly lower training time than the dense baseline.

E. NeRF Synthetic and LLFF Datasets

We also evaluate PocketGS on standard benchmarks to demonstrate its generalization capability. The per-scene results for the NeRF Synthetic dataset are shown in Table V, and the LLFF dataset results are in Table VI.

We analyze the peak memory usage of PocketGS during the MVS and training phases. The detailed per-scene memory usage is provided in Table VII, demonstrating that our system operates well within the memory budget of commodity mobile devices.

We conduct ablation studies to evaluate the impact of our core components. The following tables provide the detailed per-scene metrics for each ablation configuration, serving as

Scene	3DGS-SFM-WK					3DGS-MVS-WK					PocketGS (Ours)				
	PSNR \uparrow	SSIM \uparrow	LPIPS \downarrow	Time (s) \downarrow	Count \downarrow	PSNR \uparrow	SSIM \uparrow	LPIPS \downarrow	Time (s) \downarrow	Count \downarrow	PSNR \uparrow	SSIM \uparrow	LPIPS \downarrow	Time (s) \downarrow	Count \downarrow
Pier	20.23	0.498	0.495	156.0	35800	20.54	0.695	0.312	519.6	200936	20.29	0.625	0.329	212.8	176804
Chair	22.13	0.542	0.421	174.0	39420	21.34	0.699	0.270	555.1	180664	22.39	0.670	0.256	240.7	176970
Flowerpot	20.93	0.595	0.424	168.0	32415	21.00	0.730	0.281	486.9	242616	21.97	0.725	0.225	265.7	241976
Shrub	18.88	0.507	0.481	204.0	37476	18.53	0.582	0.427	546.7	98616	18.94	0.609	0.331	230.0	174278
Transformer	20.49	0.542	0.465	162.0	27678	19.66	0.636	0.360	546.7	122117	21.05	0.636	0.315	209.7	126222
Sofa	14.26	0.611	0.558	28.6	38	25.32	0.870	0.222	525.4	312949	24.90	0.873	0.192	389.4	289848
Table	19.71	0.754	0.382	78.0	18873	15.01	0.727	0.365	401.9	113738	22.85	0.852	0.194	184.6	179940
Robot	22.90	0.807	0.285	114.0	20795	22.21	0.862	0.207	581.7	209226	24.64	0.850	0.167	291.9	194881
Desk	20.31	0.754	0.313	72.0	20735	17.42	0.750	0.279	491.9	111202	22.03	0.838	0.172	192.8	108018
Elebox	26.17	0.922	0.197	22.4	4410	21.11	0.899	0.181	575.8	52654	27.75	0.936	0.136	255.1	37182
audio	26.05	0.815	0.330	150.0	28628	23.97	0.852	0.263	520.0	147733	27.69	0.857	0.166	270.2	155278
bag	23.71	0.855	0.313	108.0	22584	21.35	0.865	0.260	533.0	170320	24.79	0.859	0.210	320.4	179101
fireExtin	23.94	0.879	0.274	96.0	18162	22.09	0.886	0.239	592.0	146224	26.40	0.896	0.170	279.8	123325
printer	22.56	0.804	0.376	59.8	10368	20.08	0.834	0.277	542.8	203770	26.30	0.882	0.202	282.6	196896
shelf	20.39	0.761	0.418	24.8	4860	21.17	0.811	0.313	518.8	77940	25.40	0.872	0.226	224.4	75872
umbrella	24.29	0.813	0.341	47.4	9736	21.98	0.845	0.273	581.8	179388	23.30	0.826	0.235	261.9	173587
Average	21.16	0.687	0.398	112.8	23486	20.85	0.781	0.281	534.5	165367	23.67	0.791	0.225	255.2	168009

TABLE IV: MobileScan dataset comparison. Best results are highlighted in bold

Scene	3DGS-SFM-WK					3DGS-MVS-WK					PocketGS (Ours)				
	PSNR \uparrow	SSIM \uparrow	LPIPS \downarrow	Time (s) \downarrow	Count \downarrow	PSNR \uparrow	SSIM \uparrow	LPIPS \downarrow	Time (s) \downarrow	Count \downarrow	PSNR \uparrow	SSIM \uparrow	LPIPS \downarrow	Time (s) \downarrow	Count \downarrow
Chair	22.11	0.869	0.154	90.0	14433	25.37	0.957	0.054	692.4	60859	23.70	0.870	0.089	85.7	49857
Drums	18.78	0.762	0.268	53.8	12842	21.27	0.861	0.154	570.1	60640	20.97	0.775	0.183	130.1	58511
Ficus	19.99	0.812	0.212	44.2	1511	20.36	0.804	0.233	144.3	5674	22.94	0.879	0.134	33.5	5638
Hotdog	23.13	0.829	0.236	84.0	9703	29.09	0.966	0.050	571.3	40686	28.07	0.940	0.094	78.8	38583
Lego	22.02	0.795	0.228	132.0	29883	25.47	0.930	0.092	770.3	73821	24.92	0.872	0.124	130.5	74572
Materials	21.21	0.779	0.254	120.0	6934	22.45	0.843	0.170	414.8	51456	22.85	0.842	0.158	117.4	52137
Mic	23.62	0.859	0.205	31.7	5879	27.11	0.936	0.066	519.5	39553	26.24	0.901	0.120	81.0	36082
Ship	23.14	0.696	0.386	114.0	15006	24.60	0.798	0.202	574.5	69482	24.87	0.781	0.248	153.9	64208
Average	21.75	0.800	0.243	83.7	12024	24.47	0.887	0.128	532.1	50271	24.32	0.858	0.144	101.4	47449

TABLE V: NeRF Synthetic Dataset comparison.

the full data to support the aggregated results presented in the main paper.

F. Ablation: w/o Initialization (\mathcal{I})

This configuration removes the prior-conditioned anisotropic seeding in \mathcal{I} , reverting to isotropic initialization. The detailed per-scene results in Table VIII show a significant drop in performance, highlighting the importance of geometry-aware initialization for fast convergence.

G. Ablation: w/o Global BA

This configuration removes the GPU-native global Bundle Adjustment (BA) in \mathcal{G} , relying solely on the initial ARKit poses. The detailed per-scene results in Table IX indicate that the global BA is crucial for refining the coarse mobile poses, leading to better reconstruction quality.

H. Ablation: w/o MVS

This configuration removes the lightweight single-reference MVS in \mathcal{G} , relying only on the sparse point cloud from ARKit for initialization. The significant drop in all metrics, as shown

in Table X, demonstrates the necessity of a dense, geometry-faithful prior for achieving high perceptual quality within a limited training budget.

Scene	3DGS-SFM-WK					3DGS-MVS-WK					PocketGS (Ours)				
	PSNR↑	SSIM↑	LPIPS↓	Time↓(s)	Count	PSNR↑	SSIM↑	LPIPS↓	Time↓(s)	Count	PSNR↑	SSIM↑	LPIPS↓	Time↓(s)	Count
Fern	21.11	0.649	0.415	21.0	11436	21.36	0.707	0.335	118.2	38816	25.75	0.849	0.182	107.4	29220
Flower	22.97	0.701	0.328	114.0	22440	20.53	0.632	0.381	316.4	34914	25.06	0.818	0.187	92.0	28523
Fortress	26.51	0.744	0.321	180.0	29365	23.59	0.762	0.277	551.9	69762	27.15	0.901	0.129	91.6	67120
Horns	21.19	0.674	0.412	126.0	22335	17.42	0.626	0.432	530.9	38403	23.39	0.806	0.233	148.6	35996
Leaves	15.36	0.352	0.600	246.0	9358	15.28	0.327	0.588	190.4	20315	15.77	0.456	0.501	60.8	9358
Orchids	18.85	0.562	0.401	66.0	21968	18.11	0.593	0.353	141.1	66975	21.73	0.772	0.183	138.9	55320
Room	21.70	0.764	0.400	15.3	4737	21.34	0.787	0.358	203.4	27610	26.18	0.897	0.168	75.6	19273
Trex	20.42	0.684	0.360	96.0	21645	18.62	0.664	0.376	452.4	30104	23.33	0.830	0.194	128.6	22349
Average	21.01	0.641	0.405	108.0	17910	19.53	0.637	0.387	313.1	40862	23.54	0.791	0.222	105.4	33395

TABLE VI: LLFF dataset comparison.

Metric	audio	printer	fireExtn	flowerpot	Elebox	desk	transformer	shrub	bench	sofa	Keyboard	bike	Pier	bag	robot	umbrella	chair	table	shelf	Avg.
MVS Peak Mem. (GB)	1.55	1.50	1.55	1.48	1.38	1.19	1.48	1.64	2.22	1.39	1.67	1.50	1.73	1.42	1.57	1.56	1.49	1.24	1.47	1.53
Training Peak Mem. (GB)	2.65	2.62	2.50	2.49	2.44	2.41	2.29	2.27	2.20	2.15	2.15	2.12	2.03	2.02	1.98	1.95	1.94	1.91	1.82	2.21

TABLE VII: Per-scene peak memory.

Metric	Elebox	Pier	audio	bag	bench	bike	chair	desk	fireExtn	flowerpot	printer	robot	shelf	shrub	sofa	table	transformer	umbrella	Avg.
PSNR (dB)	27.03	20.16	20.93	22.72	21.97	23.02	22.09	22.07	26.46	20.98	24.83	21.35	24.99	18.80	22.05	22.89	20.91	21.55	22.49
SSIM	0.9335	0.6048	0.8138	0.8303	0.6859	0.7185	0.6514	0.8385	0.8961	0.6836	0.8555	0.7934	0.8647	0.5889	0.8203	0.8522	0.6255	0.7955	0.7696
LPIPS	0.1400	0.3572	0.1859	0.2628	0.3207	0.2553	0.2760	0.1726	0.1781	0.2735	0.2390	0.2259	0.2481	0.3588	0.2706	0.1935	0.3316	0.2699	0.2533
Time (s)	369.1	325.6	363.0	335.8	350.4	327.7	306.8	186.7	429.2	386.9	352.7	283.0	318.3	331.5	329.3	172.6	297.7	284.5	319.5

TABLE VIII: Per-scene metrics **w/o initialization** (removing prior-conditioned anisotropic seeding in \mathcal{I}).

Metric	Elebox	Pier	audio	bag	bench	bike	chair	desk	fireExtn	flowerpot	printer	robot	shelf	shrub	sofa	table	transformer	umbrella	Avg.
PSNR (dB)	27.61	20.21	26.95	24.47	22.40	23.03	22.30	22.02	26.45	21.67	26.10	24.38	24.85	18.82	24.49	22.52	20.80	23.01	23.45
SSIM	0.8975	0.5910	0.8156	0.8201	0.6869	0.6832	0.6318	0.8014	0.8548	0.6843	0.8401	0.8048	0.8282	0.5774	0.8283	0.8107	0.5915	0.7825	0.7517
LPIPS	0.1350	0.3253	0.1743	0.2172	0.2857	0.2595	0.2639	0.1758	0.1821	0.2326	0.2093	0.1869	0.2367	0.3311	0.1928	0.2026	0.3285	0.2437	0.2324
Time (s)	230.7	212.2	280.5	311.5	259.9	231.9	233.5	181.3	285.0	254.2	282.5	263.2	232.0	230.6	352.7	176.7	238.5	263.0	251.1

TABLE IX: Per-scene metrics **w/o global BA** (removing GPU-native global BA in \mathcal{G}).

Metric	Elebox	Pier	audio	bag	bench	bike	chair	desk	fireExtn	flowerpot	printer	robot	shelf	shrub	sofa	table	transformer	umbrella	Avg.
PSNR (dB)	23.10	18.25	24.43	23.67	19.84	21.03	19.46	20.12	23.35	19.56	23.38	22.66	21.09	16.98	21.96	19.61	18.91	21.92	21.07
SSIM	0.9029	0.3181	0.7425	0.8163	0.4339	0.5333	0.3467	0.7574	0.8413	0.5089	0.8195	0.7925	0.7845	0.2820	0.7690	0.7533	0.4489	0.7795	0.6461
LPIPS	0.2113	0.6392	0.3905	0.3201	0.5653	0.4897	0.5609	0.2855	0.3064	0.4894	0.3259	0.2600	0.3583	0.6229	0.3898	0.3478	0.5480	0.3366	0.4137
Time (s)	122.2	93.8	186.7	142.1	101.4	110.7	129.0	95.9	178.5	118.9	149.3	112.2	142.3	88.2	136.2	89.9	111.0	137.5	124.8

TABLE X: Per-scene metrics **w/o MVS** (removing lightweight single-reference MVS in \mathcal{G}).